

GEOPHYSICS®

Deep-learning EM monitoring coupled to fluid flow simulators

Journal:	<i>Geophysics</i>
Manuscript ID	GEO-2019-0428.R1
Manuscript Type:	Machine Learning and data analytics for geoscience applications
Keywords:	electromagnetics, neural networks, reservoir characterization, monitoring
Area of Expertise:	Electrical and Electromagnetic Methods, Reservoir Geophysics

SCHOLARONE™
Manuscripts

Deep-learning EM monitoring coupled to fluid flow simulators

Daniele Colombo¹, Weichang Li², Ernesto Sandoval-Curiel¹ and Gary W. McNeice¹

Running Head: Deep learning EM reservoir monitoring

¹*Geophysics Technology, EXPEC Advanced Research Center, Saudi Aramco*

²*Aramco Research Center – Houston, Aramco Services Company, USA*

daniele.colombo@aramco.com; weichang.li@aramcoservices.com;
ernesto.sandovalcuriel@aramco.com; gary.mcneice@aramco.com

ABSTRACT

Reservoir characterization and monitoring represent some of the most ambitious goals for geophysical methods. Several challenges are involved including sensitivity to the parameter changes and resolution of the obtained results. Electromagnetic (EM) methods are attractive for reservoir applications due to the high sensitivity of the resistivity parameter to oil/water saturations. Cross-well EM and surface-to-borehole EM provide opportunities for reservoir monitoring. The EM inverse problem, however, is highly non-convex and ill-posed such to necessitate significant preconditioning in the form of a-priori information and regularization that impact resolution. We explore the use of machine-learning (ML) techniques in the form of deep learning neural networks for implementing EM-based reservoir monitoring coupled with a dynamic fluid flow simulator. A cross-well acquisition setup is modeled in the framework of a realistic water-alternating-gas (WAG) reservoir simulation scenario for enhanced oil recovery (EOR). Several reservoir saturation instances are generated, converted into resistivity and corresponding cross-well EM data are generated using an electric source and a multicomponent (electric-magnetic) receiver assemblage. The U-Net deep learning network is modified for the purpose of training and validation where saturation models and corresponding EM data are used. We also test the sensitivity of the deep learning inversion to multiple EM components, noise in the data, generalization problem and 3D reconstruction ability where we use 3D convolutional neural network (CNN) layers. In all cases, ML inversion proves to be robust with good resilience to increased noise levels. Prediction results show excellent reconstruction capabilities with resolution comparable to the reservoir models used by the simulator. Results suggest that ML inversion through deep learning can become an efficient approach to data-driven and physics-constrained

reservoir monitoring where the sensitivity of the EM-based techniques to fluid saturations can be fully exploited without compromising the resolution and accuracy of the results.

Downloaded 11/18/19 to 128.119.168.132. Registration subject to <http://library.seg.org/>. Terms of Use at <http://library.seg.org/>.

INTRODUCTION

Reservoir monitoring of the production process is one of the most important objectives for geophysical methods and one of the most difficult to implement. Geophysical methods can in principle help reservoir management by detecting and mapping in the interwell space the fluid saturation variations related to production. Some of the most common recovery techniques are based on waterflooding where water (e.g., seawater) is injected at the periphery of the reservoir to sustain production. Other enhanced recovery techniques (EOR) consist of water-alternating-gas (WAG) where water injection may be alternated with CO₂ injection for example. In all cases they produce a time-dependent variation of the saturation patterns in the reservoir. Electromagnetic methods with a controlled source are amongst the best candidates to complement engineering operations with geophysical data due to the large sensitivity of the resistivity parameter to fluids.

It is generally recognized that the most promising deep-looking EM techniques for reservoir monitoring should be based in the borehole such as cross-well EM (Wilt et al., 1995) or a combination of surface and borehole acquisition setups such as surface-borehole EM (Colombo et al., 2018) or borehole-surface EM (He et al., 2004; Tietze et al., 2015; Villamajo et al., 2015). Such configurations mitigate the problem of the rapid decay of the EM radiation with frequency in conductive formations (i.e., the skin depth effect) causing a loss in resolution and in reconstruction ability. Results of successful EM applications for reservoir monitoring have been shown in various publications (Marsala et al., 2008; McNeice and Colombo, 2018) where problems of measurement repeatability, effect of steel infrastructures, sensitivity of EM field components and corresponding polarizations have been discussed (Tietze et al., 2015; Villamajo et al., 2015; Streich, 2016; Puzyrev et al., 2017; Colombo and McNeice, 2018). In many cases, the

1
2
3 adoption of specific processing and acquisition strategies allows to alleviate the problem and
4 produce useful results.
5
6

7
8
9 A more general problem affecting EM measurements, as well as other geophysical methods, is the
10 inversion of measured data for the model parameter distribution. The EM inversion problem is
11 highly non-convex and ill-posed such that it requires the introduction of various constraints and
12 heavy regularization. In most cases, a good starting model is needed to satisfy the linearization
13 assumptions of deterministic inversions. These steps are highly subjective and depend on the
14 experience of the geophysicist doing the work. Despite the limitations, the theoretical development
15 around inverse problems has been extensive and the existing results prove that, with the right
16 algorithmic strategies, adequate resolution and robust results can be obtained from single
17 inversions (Abubakar et al., 2009) or multi-physics joint inversions (Liang et al., 2016). This is the
18 mainstream and the benchmark.
19
20

21
22
23
24
25
26
27
28
29
30
31 A new area of ongoing research is represented by machine learning (ML) as applied to geophysical
32 problems. Several works have been published in recent times where the most common applications
33 involve classification of geological structures for interpretation through supervised learning
34 (Guillen et al., 2015), unsupervised learning (Di et al., 2018), or a combination of the two (Li,
35 2018). ML using deep learning or variations of convolutional neural networks (CNNs) is also an
36 attractive approach for data-driven inversion. This area of research is still relatively new with
37 applications detailed on marine controlled-source EM (CSEM) for salt delineation (Oh et al.,
38 2018), reflectivity inversion (Kim and Nakata, 2018), seismic tomography and velocity model
39 building (Araya-Polo et al., 2018; Wang et al., 2018), or inversion schemes incorporating ML to
40
41
42
43
44
45
46
47
48
49
50
51
52
53
54
55
56
57
58
59
60

1
2
3 learn optimal descent directions such as in the Supervised Descent Method without computing the
4 Jacobian or Hessian matrices (Xiong and De la Torre, 2013; Guo et al., 2018). The attractive traits
5 of ML/deep learning, when applied as an inversion scheme, are related to the capability of deriving
6 high-complexity nonlinear mapping functions from input models and data (training phase) to
7 output models, where any complex nonlinear operator can be approximated by deep neural
8 networks (Hornik et al., 1989). Deep learning allows the efficient sampling of the model and data
9 spaces if the probability distribution of models is known a-priori (Goodfellow, 2016). Multiple
10 information not related to known physical relations can be easily incorporated into the problem to
11 infer new parameter distributions (Colombo et al., 1997) and to limit the nonuniqueness of the
12 results.
13
14

15 Most of the ML inversion schemes utilized in geophysical applications to date consist of a “fully
16 learned reconstruction” approach (Adler and Öktem, 2017), which consists of learning the
17 pseudoinverse operator directly from the data. This presents a disadvantage that is identified in the
18 need of performing sufficient training to adequately sample the model and data spaces. The
19 prediction phase is a heuristic process that is as good as the training performed. It is typically
20 accurate when the searched model falls within the boundaries of the explored spaces and may fail
21 when models and data fall outside of the training boundaries or when models are not part of some
22 underlying manifold. With such conditions it is easy to envisage the limits and the best
23 applicability of such an approach that is more suited for reconstruction of gaps in a more or less
24 continuous distribution, for example the image inpainting for filling holes in photographs (Liu et
25 al., 2018), rather than for predicting unforeseen distributions of parameters. Therefore, ML
26 inversion is hardly applicable for reconstructing models for which we do not have any a-priori
27
28
29
30
31
32
33
34
35
36
37
38
39
40
41
42
43
44
45
46
47
48
49
50
51
52
53
54
55
56
57
58
59
60

information, or we do not know anything about the probability distribution. In such a case, the model space would need to be sampled with a large set of modeling exercises and we would never be confident enough to have explored the model space sufficiently. In such conditions, deep learning would quickly lose its appeal as an efficient and robust inversion method. Conversely, if assumptions are made about the probability distribution of the model parameters for real world applications, then ML can help in efficiently sample models and data to find the reciprocal relations and predict adjoining distributions.

In the application of ML inversion discussed in the present paper we approach the problem of reservoir monitoring using EM methods (cross-well EM in the specific case), due to the high sensitivity to saturation variations in the reservoir. We link the EM approach to a fluid flow simulator (reservoir simulator) to generate several instances of fluid saturations corresponding to a WAG process and by generating the corresponding EM responses for each case. We use the time dimension of the reservoir simulator to sample a large range of saturation models, where several parallel, through time, simulations can be achieved by changing the initialization parameters of the simulator to cover several case scenarios. Reservoir models are regularly updated by reservoir engineers through history matching of production data and new wells. Reservoir simulators are also subject to the physics of the dynamic fluid flow in porous media and the corresponding models can be considered the best educated guess of the fluid distribution at any given time. As such, they represent an optimal training source for a deep learning network. The so-created nonlinear mapping functions can then be used to predict saturation patterns in the interwell space given a set of geophysical EM measurements. High-resolution parameter distributions (comparable to the reservoir model scale) are needed for this purpose to integrate the results with the simulator. In

this paper we describe, with realistic synthetic examples, the framework for implementing deep learning EM inversion for reservoir monitoring coupled to fluid flow simulators. We also explore the sensitivity of ML inversion to different EM field polarizations, variable amount of noise, 2D versus 3D reconstructions, random partition vs. forward extrapolation of models, and compare the results between ML and a standard least-square inversion approach.

MACHINE LEARNING INVERSION

The approach we implement in this paper is an automatic supervised learning where we have access to input-output pairs (not available in unsupervised learning). These sample pairs are represented by fluid saturation distributions in the reservoir, as generated by several realizations of a dynamic fluid flow simulator, and the corresponding simulated EM fields. Our approach falls under the definition of “fully learned reconstruction” (Adler and Öktem, 2017) where the parametric pseudoinverse operator is learned directly from the data.

ML inversion is analogous to conventional geophysical inversion in the sense that it aims at converting information from observations (data space/input) to property distributions (parameter or model space/output) where a performance criterion is optimized based on statistical analyses from example data or past experience (Alpaydin, 2009). Given the formulation of an inverse problem such as:

$$\mathbf{y} = \mathbf{H}\mathbf{x} + \mathbf{e}, \quad (1)$$

where \mathbf{H} is a forward operator, \mathbf{y} is the vector of observed data, \mathbf{x} is the vector of the unknown parameters and e represents the noise in the data, the objective is to solve for the parameter vector \mathbf{x} . A least-square solution can be sought for an objective function of the form:

$$\Phi = \|\mathbf{H}\mathbf{x} - \mathbf{y}\|_{L_2}^2 \quad (2)$$

For the ML inversion case, the objective function can be written as (Kim and Nakata, 2018):

$$\Phi_{\text{learn}} = \|\mathbf{H}_{\Theta}^{\dagger} \mathbf{y}_n - \mathbf{x}_n\|_{L_2}^2 \quad (3)$$

where Θ is the network model parameter set optimized during the learning process, the term $\mathbf{H}_{\Theta}^{\dagger}$ is a pseudoinverse operator (or nonlinear mapping function) parameterized by Θ (Adler and Oktem, 2017), \mathbf{x}_n is the target dataset (e.g., true resistivity model), $\mathbf{H}_{\Theta}^{\dagger} \mathbf{y}_n$ is the predicted output dataset (e.g., reconstructed resistivity model) based on the input to the network \mathbf{y}_n (e.g., EM field data). The misfit between the target and the predicted datasets (loss function Φ) is minimized to obtain an optimized set of network parameters Θ during the training phase. The minimization leads to a set of nonlinear feature representations of the inputs with weights and biases that define the pseudoinverse operator $\mathbf{H}_{\Theta}^{\dagger}$. This operation performs the deep learning inverse mapping from the data space into the parameter space. The optimization embedded in the ML inversion requires training over a large number of representative samples. This enables the network model to build adequate capacity to represent the complexity of the task and to avoid at the same time the problem of overfitting. When this is not possible, the network model may suffer from overfitting with effects similar to an ill-posed geophysical inverse problem. While in ill-posed inversions non-uniqueness and small changes in the input data may result in large changes in the reconstructed

parameters, an overfitted deep learning network model may lead to large prediction (i.e., testing) errors even if a very good fit is provided on training samples. This corresponds to the lack of generalization of the network model. The strategies adopted in ML to decrease the testing errors are known collectively as regularization and include a wide variety of strategies. The regularization techniques implemented in this work consist of: weight regularization, dropout and data augmentation. Weight regularization is similar to regularization techniques used in geophysical inversion and consist of the implementation of Lagrange functions with penalty terms weighted by hyperparameters (i.e., Lagrange multipliers) that are added to the standard objective function. Dropout techniques offer a computationally efficient and often effective regularization strategy for reducing overfitting and improving generalization performance. These are implemented on a per-layer basis in a deep neural network. During training, some number of layer outputs are randomly ignored or “dropped out”. This has the effect of making the training process “noisy” by simulating a sparse activation from the layer, and by breaking up situations where network layers co-adapt to correct mistakes from prior layers. Dropout techniques make the network model more robust. Data augmentation consist of the creation of fake and plausible datasets to augment the training base and enhance the generalization capability of the network model.

Differently from geophysical inversion techniques, the forward operator in ML inversion may not be specific to explicit physics bases, such as in the case of the fully learned reconstruction discussed here. The mapping functions from the data to the model space are nonlinear consisting of a deep series of neural network layers and nonlinear activation functions. Geophysical inverse problems are solved in most cases through linearization as a local optimization technique. The ML inversion can explore the model space much better than a linearized inversion as long as the model

space is adequately sampled and the training set represents a realistic and extended range of model and data corresponding to the real cases.

EXPERIMENTAL SETUP

We simulate a WAG process for EOR consisting of highly conductive seawater and CO₂. The fluid saturations in the reservoir are obtained through the use of a reservoir simulator (Dogru et al., 2009) where reservoir saturation snapshots are taken at regular time intervals over a period of 10 years. Saturations are then converted into the resistivity parameter using an accurate porosity model with Archie's relation (Archie, 1952) and parameters characteristic of the reservoir. The acquisition setup consists of a cross-well EM experiment with two vertical wells (Figure 1) where the well on the left is the injector and contains the sources while the well on the right is the observation well. The separation between the two wells is 120 m. The source is represented by a vertical current dipole (J_z) of unit moment with vertical sampling of 1.0 m and a transmitted frequency of 1,000 Hz. The receiving setup consists of a four-component sensor array comprising one vertical electric (E_z) and three-component magnetic sensors (H_x , H_y , H_z). By observing the reservoir depth slice at different time intervals and by comparing the WAG process to the baseline where only waterflooding is active, we can conclude that the resistivity variations in the reservoir due to the WAG process are significant. We should consider that the reservoir simulator was run also considering the simultaneous occurrence of the waterflooding such that the two effects of background waterflooding and WAG are both represented by the models.

For each fluid flow simulation realization we upscale the simulator pillar grid into an adaptive 3D finite-difference (FD) mesh and calculate the corresponding EM fields using a 3D FD method (Commer and Newmann, 2008). Models and data are differentiated relative to the baseline to focus the attention on the time-lapse changes in resistivity and signal strength (Figure 2 and Figure 3). Electric and magnetic responses are concisely represented for each simulated model by plotting amplitude and phase as a function of source (x-axis) and receiver (y-axis) positions. By analyzing the differential signal plots we observe that E_z forms a well-defined crossing pattern indicating a high spatial sensitivity from both the source and receiver sides: J_z - E_z combination (Figure 2 f-g). The two differential amplitude responses for the case of WAG at Year 3 and Year 6 time-lapse model are very different suggesting good sensitivity of the modeled EM fields to the resistivity parameter variations. The magnetic field distribution shows a different behavior with most of the response concentrated in the H_y components (coupled to the vertical electric source J_z) but with some signal also distributed on the other two components (H_x, H_z) as a result of the 3D resistivity distribution (Figure 3). We can notice that while the H_y component shows good sensitivity to the reservoir time-lapse variations, the appearance of the amplitude plots is different relative to E_z forming mainly vertical stripes influenced by the electric source and a weak cross pattern from the magnetic receiver side. The spatial resolution of the magnetic field is lower than the vertical electric for which the necessity of conserving the vertical current density produces sharp variations of E_z at each resistivity boundary (Colombo et al., 2018). Data and models in form of 2D images are then used for training, validation and testing of the deep learning network.

DEEP LEARNING NETWORK

A reservoir model is predicted through deep-learning network system modified from a U-Net architecture. The U-Net (Ronneberger et al., 2015) was initially developed for biomedical image segmentation where the training sets are typically limited in number. The network consists of a contracting path and an expansive path. The contracting path consists of repeated application of convolution, nonlinear activation via rectified linear unit (ReLU) with batch normalization and max-pooling operation, with increased filter depth. As a result, the spatial information along the contraction path is reduced while the extracted feature information is enriched. The expansive path combines the feature and spatial information through a sequence of upsampling and concatenations of the features obtained from the contracting path, with increasing resolution. The advantage of this type of structure is the potential to retain the spatial information at different scale and resolution of the input, and at the same time to extract features capable of representing sample at different levels with increasing complexity. To turn U-Net into an inversion operator, we have replaced the final layer from the pixel-wise softmax combined with the cross-entropy loss function for segmentation to a mean squared error (MSE) loss function between the predicted and the true resistivity models. An additional modification consists of removing the “copy and concatenate” of lower-level features when such a linkage poses restrictive mapping constraints, or it becomes impractical when the input and output dimensions are very different, e.g., later in mapping 3D resistivity from 2D electromagnetic field data. Essentially, the deep learning network takes an image (input fields) to image (output resistivity model) translation perspective, as shown in Figure 4.

The contracting path learns the abstract representation of the input field data at various scales and the expansive path combines these features to produce a subsurface resistivity model. More specifically, for 2D field data to 2D resistivity inversion, the network takes multichannel fields (E_z , H_x , H_y , and H_z , real and imaginary parts or magnitude and phase) all down sampled to size 96×96 , and feeds through a series of convolutional blocks as described earlier with spatial dimension of the feature space subsequently reduced to 48×48 , 24×24 , 12×12 and 6×6 , while the depth (the number of filters) is increased from 12 to 24, 48, 96 and 192. The expansive path reverses this process with the goal to minimize the MSE between the predicted resistivity and the true resistivity of the training samples. In the network shown in Figure 4 we display the decomposition of one field component down sampled to size 96×96 ($\times 2$ for amplitude and phase), from the WAG model truncated between 60-203 depth samples.

Given the limited number of reservoir fluid simulations we apply excessive data augmentation (Dosovitskiy et al., 2014; Ronnerberger et al., 2015) by interpolation of fluid flow simulation models with all the other models through a combinatory mechanism. The surrogate data allow the network to learn invariance relative to much extended saturation scenarios. A similar process can be implemented to introduce random geologic uncertainties (e.g., fracture corridors) or other random parameter deformations and translations to allow the network to learn invariance to them.

RESULTS

We performed a number of reconstruction tests where we used a total of 194 simulated fluid models and corresponding EM responses. For the 2D cases the available dataset was partitioned

in 154 samples for training, 20 samples for validation, where the loss function consists of the MSE minimization between true and predicted differential resistivity, and 20 samples for testing. Samples were selected randomly. The corresponding EM responses were then evaluated first with E_z components only (amplitude and phase of the differential response) and then as the combination of E_z with all the other magnetic channels: H_x , H_y , H_z . The effects of noise in the data were then evaluated as well as the sensitivity of the procedure to forward time extrapolated models versus models falling within the boundaries of the distribution (generalization test). Finally, we evaluated the deep learning network capability of reconstructing the 3D resistivity distribution around the two wells.

Electric versus Electric+Magnetic

We first analyzed the reconstruction performances of the deep learning network using only the E_z component that showed the largest spatial resolution among the EM components modeled. After validation, the trained network model was applied to the 20 E_z modeled data left apart for testing and the associated unknown resistivity models were predicted. Since the test samples were not utilized neither for training nor for validation, the obtained performance represented the network predictive capability (Figure 5).

The obtained results provide a highly accurate reconstruction of the fluid-related resistivity distributions in the model where the average model RMS (RMSm) between true and reconstructed models is 0.33 Ohm·m for all the 20 reconstruction cases considered together. A comparison between the current results of ML inversion and a corresponding conventional least-square

inversion test (Figure 6) was performed on the same acquisition setup but with only CO₂ simulated injection (Colombo and McNeice, 2017), which shows that ML inversion is far superior in terms of accuracy of the reconstruction and achievable resolution (RMSm=5.93 Ohm·m for least-square inversion). These results are consistent with what was obtained by other authors where ML-inversion applications achieve higher resolution than any conventional inversion scheme such as least squares (Adler and Öktem, 2017; Kim and Nakata, 2018).

The next example is relative to the combination of the electric and magnetic data. It has been shown by Colombo and McNeice (2013) that E_z is the EM field component with the largest spatial resolution and with large sensitivity to the model parameters. The magnetic field component H_y is the component coupled with the J_z source and correctly shows the largest signal variation based on the differential amplitude plots (Figure 3). The combination of electric and magnetic channels should be beneficial in order to augment the data redundancy: six more channels in input with a total of eight. Added sensitivity, especially to conductive parts of the model, is also expected with a possible decrease in spatial resolution, as discussed earlier.

We compare models trained with E_z component only versus E_z plus H_x, H_y, H_z as the input, where the output remains the same. The case with all the available EM field data converges much faster (around 65 epochs) than the case with E_z only (350 epochs). The model losses, both training and validation, are significantly smaller in the E_z plus H_x, H_y, H_z trained case (Figure 7). Prediction performance on testing samples shows better results when the model is trained on the full field data (Figure 8) obtaining even higher resolution and accuracy in model reconstruction for the independent testing cases (RMSm=0.275 Ohm·m) than the E_z only case (RMSm=0.330 Ohm·m).

Noise effects

We want to explore how noise applied to the data affects the deep learning prediction. Previous studies have shown that training with noise is equivalent to imposing a regularization to the derivation of the CNN nonlinear mapping functions (Bishop, 1995). It has also been shown that training with noise can improve the network generalization characteristics (Sietsma and Dow, 1991) by optimizing the tradeoff between the bias and the variance of a model, or, in other words, by preserving adequate capacity and reducing at the same time the risk of overfitting (Bishop, 1995; Goodfellow et al., 2016).

A Gaussian noise distribution is applied to the data with variable standard deviations. Estimation of reliable levels of noise is not straightforward. The modeled data are unit moment; therefore, the level of signal can be linearly scaled by augmenting the source moment. For the type of data we modeled, we assume that the sensitivity for an electric field sensor is in the range of $10^{-9} V/\sqrt{Hz}$ and we define three zero-mean Gaussian noise levels with standard deviations of $10^{-9} V/\sqrt{Hz}$, $5 \cdot 10^{-9} V/\sqrt{Hz}$, and $10^{-8} V/\sqrt{Hz}$. The noise level for the magnetic data is considered the same as per the electric field given that the unit moment signal ranges are comparable between E and H channels (Figure 2, Figure 3). A visual representation of the noise levels (Figure 9) indicates the severity of the operation where the weaker signal is progressively affected and masked by the increasing noise threshold. Training, validation and testing are performed separately for the three selected levels of noise and using all the EM field components available. Results of the prediction (Figure 9 – right column) are provided for one resistivity snapshot where the case with no noise is

1
2
3 shown alongside with the predicted resistivity models corresponding to noisy data. The
4 deteriorating effects of increasing noise can be seen as distortions at high resolution detail levels,
5 while the baseline large variations are less sensitive to noise.
6
7

8 Two dominant effects during training and validation are consistently caused by increased noise
9 levels. These include 1) slower convergence with longer number of epochs, and 2) increased loss
10 levels for both training and validation at convergence. With clean data or very low noise levels (
11 $10^{-9} V/\sqrt{Hz}$), the training phase arrived at convergence in less than 100 epochs. As the noise
12 level increases to $5 \cdot 10^{-9} V/\sqrt{Hz}$, and $10^{-8} V/\sqrt{Hz}$, the training phase takes significant larger
13 number of epochs to converge with larger loss levels at convergence for both training and
14 validation (Figure 10). During the training and validation phases, we have chosen the stop criteria
15 to be determined when no decrease in validation loss for ten consecutive epochs is recorded. This
16 early stopping approach can be considered also as a regularization technique implemented to avoid
17 overfitting and to ensure, at the same time, the testing accuracy. The corresponding RMSm values
18 averaged over all resistivity model pixel locations are summarized in Table 1.
19
20

21 Forward time extrapolation

22
23
24
25
26
27
28
29
30
31
32
33
34
35
36
37
38
39
40
41
42
43
44
45
46
47
48
49
50
51
52
53
54
55
56
57
58
59
60

Downloaded 11/18/19 to 128.119.119.168. Redistribution subject to SEG license or copyright; see Terms of Use at <http://library.seg.org/>.
In the previous tests we have randomly sampled training, validation and testing sets from the same
underlying probability distribution of saturation models and EM data by honoring the statistical
learning assumption that sets need to be independent from each other and that the training set and
the test set are identically distributed (Goodfellow et al., 2016). The underlying assumption is that
the reservoir simulator with all its built-in constraints (physics, production data, geology, etc.)
governs the range of possible saturation realizations, and that the randomly selected training

samples have a sufficient representation of all the data-model mapping scenarios, including those anticipated from the independent testing cases. We want to test in this section the generalization capability of the derived pseudoinverse operator or, in other words, the ability of the prediction to perform well on a set of reservoir fluid distributions outside of the model space used for training and validation. More specifically, instead of randomly partition the entire set of 194 samples over the whole time horizon into 134 training, 30 validation and 30 testing samples, we first divide the samples into two time segments, one from early time window consisting of 164 samples, which are then randomly partitioned into 134 training samples and 30 validation samples, and the other from a later time window consisting of 30 samples for testing. This configuration allows us to test scenarios where the future reservoir model variations to be tested may not have a full representation by the training set which is from an early time period. In a way, this simply adds a chronological order to the sample partition so that we could verify the generalization ability of the predictor in the context of continuous monitoring over time.

We ran the forward time extrapolation configuration for the clean data, as well as for the cases with added noise described previously. The prediction results are shown in Figure 11 for one representative sample while the average numerical reconstruction errors for all the testing samples have been included in Table 1. The joint analysis of the images and of the numerical reconstruction errors indicate that the prediction capability for the forward extrapolation case is worse when compared to the random sample partitions, and it further deteriorates as the noise level increases. The RMS_m values for the testing cases are higher in the forward extrapolation than in the random partitioning cases while preserving an overall good prediction capability. The fine details of the saturation-related resistivity structure are masked by the increasing levels of noise while the main

1
2
3 features are maintained. The overall effect is that of an increasing regularization on the prediction
4 results as also indicated by the larger model loss for higher levels of noise in the data (Figure 12).
5
6

7 Even in these adverse conditions of forward time extrapolation and high noise levels, results
8 indicate a good generalization capability of the pseudoinverse operator showing overall high
9 capacity and small bias.
10
11

12 **3D case**

13

14 The cross-well EM data are primarily sensitive to the distribution of resistivity between the
15 transmitter and receiver well pairs. Given that the injected fluid is also expanding laterally, the
16 same 2D electromagnetic dataset provides sensitivity to the surrounding 3D resistivity structure
17 changing over time. The problem is difficult to solve through a linearized least squares inversion
18 approach as the number of unknowns are rapidly increasing and the inverse problem is ill-posed.
19 While in the previous tests we have used the 2D EM dataset to reconstruct only the central slice
20 connecting the wells, here we address the challenge of directly predicting the variations of the 3D
21 resistivity model around the wells as resulting from the WAG injection process.
22
23

24 We need more data to solve for more variables, hence more training sets for more variables to be
25 solved. We then use all the available E and H field component data for this purpose with the
26 augmented dataset. A total of 194 samples were partitioned into 134 training, 30 validation and 30
27 testing samples. The additional augmented data were generated through combinatorial
28 arrangement of reservoir simulation models. We extended the modified 2D U-Net model to the
29 3D case by introducing a flattening and fully connected layer in the middle of the contracting and
30
31

expansion paths, where the expanding path consists of 3D CNN layers (Ji et al., 2013). Figure 13 shows the learning behavior of the network in terms of the training and validation losses. The training phase converges in about 25 epochs with a converged RMSm level evaluated on the testing samples at around 0.42 Ohm·m where no noise is applied to the data in this case (Table 1). The visual analysis of the prediction results provide evidence of the accuracy and robustness of the reconstruction also in the 3D case (Figure 14).

The summary of the results (Table 1) suggest that the deep learning EM inversion applied to a cross-well configuration performed very well under varied conditions of noise and dimensionality, always allowing to recover the underlining, saturation-related, resistivity distribution.

DISCUSSION

ML/deep learning methods applied to inverse problems can provide a valid alternative to conventional approaches. The implementation we have demonstrated corresponds to a fully learned reconstruction (Adler and Öktem, 2017) where no assumptions and no a-priori information are provided to the pseudoinverse operator that is obtained as fully data-driven. To be successful such an approach requires that the model space is adequately sampled and the searched parameter reconstruction is not too far from the training dataset. The least-square inversion counterpart is not better, meaning that any local optimization, as deriving from a linearization process, needs a good starting model, therefore, some robust a-priori information. From this point of view ML inversion proves to be more robust, higher resolution and more objective than a linearized inversion scheme.

For the specific application described, the complex non-linear basis functions are derived between input models and output data through an automatic supervised training assisted by a dynamic fluid flow simulator. The reservoir model is regularly updated with data from production and new wells such that it represents the best guess for the reservoir saturations at a given time. For the purpose of training the deep learning network various fluid flow realizations through time can be performed by changing the parameter settings or even by introducing random variables or geologic uncertainties (e.g., fracture models). Such a large constrained base of knowledge that is updated over time generates robust pseudoinverse operators that can be used to predict unforeseen saturation distributions through the generalization of the prediction functions. This is possible as we can make adequate assumptions about the probability distributions we can encounter in real-world applications (Goodfellow et al., 2016).

Synthetic tests on various amounts of random noise levels have shown a very good resilience of the derived pseudoinverse operators allowing to reconstruct in all the cases the features of interest with good resolution and robustness. Various techniques can be implemented to enhance the robustness of the deep learning inversion. These include: decreasing the resolution of the searched parameter reconstruction by making adjustments to the number of the model free parameters and/or by imposing bounds to the parameter values, introducing penalty terms in the deep learning loss function, implementing dropout techniques or early stopping criteria, and performing excessive data augmentation. These techniques are related to regularization operations that are implemented to avoid overfitting while preserving adequate model capacity, thus generalization capabilities (Bishop, 1995).

One important aspect of ML inversion through deep learning is the capability of deriving highly complex nonlinear basis functions to describe relations among features without the need of relying on physical laws to connect parameters with the observations. This property would result extremely useful for conducting reservoir studies where the complexity and multiplicity of available parameters makes stochastic integration approaches computationally prohibitive and deterministic ones weak with high risks of ending inversions in local minima. The capability of integrating multiple data types at once reduces the nonuniqueness of the results and deep learning inversion approaches are optimally suited to achieve this objective.

As a continuation of the study we will apply what we learned from the synthetic case to real datasets such as cross-well EM and surface-to-borehole EM. Deviations from the case presented will involve considerations about additional noise sources (nonrandom) or signal distortions such as related to casing and metal infrastructures. Additional data reduction, conditioning and calibration are expected to be necessary before the network could be effectively trained with the reservoir simulator and the obtained training results could be applied to measured EM data.

CONCLUSIONS

Recent developments and applications of surface-to-reservoir controlled-source EM and cross-well EM have shown the feasibility of performing reservoir fluid saturations monitoring. The highly sensitive EM data to saturations suffer however of low resolution other than of a highly non-convex and ill-posed inversion problem. ML inversion techniques through the adoption of

1
2
3 deep learning networks can address some of these problems. When compared to conventional
4 inversion approaches, ML can provide robust results of higher resolution, it is not tied to
5 simplifications of the problem, such as linearization, and uses complex nonlinear functions to map
6 models and data reciprocal relations for generating pseudoinverse prediction operators. Several
7 parameters not related to common physical processes are naturally incorporated into the solution
8 to help the stabilization and improve the uniqueness of the parameter reconstruction. The limit of
9 the presented approach lies in the necessity of performing a sufficient number of simulations to
10 appropriately sample the model space and allow the derivation of robust nonlinear basis functions.
11 Such a limitation can seriously affect the prediction of completely unknown parameter
12 distributions, such could be the case of an exploration scenario in a frontier area. The problem is
13 less significant in the case of reservoir monitoring where a-priori information is available such as
14 provided by well logs, production data and seismic stratigraphy. In such conditions, and through
15 the support of physically-constrained dynamic fluid flow simulators, ML inversion can provide
16 the mechanism to perform history matching between geophysical data and reservoir models. With
17 specific reference to EM-based monitoring techniques, ML can potentially boost the resolution of
18 parameter reconstruction allowing to fully exploit the sensitivity of the EM-based techniques to
19 fluid saturations.

ACKNOWLEDGMENTS

20
21 The authors wish to thank Lin Liang, an anonymous reviewer and the associate editor Aria Abubakar for
22 their suggestions, which helped in improving the quality and accuracy of the manuscript.

1
2
3 **REFERENCES**
4
5
6
7

8 Abubakar, A., T. M. Habashy, M. Li, and J. Liu, 2009. Inversion algorithms for large-scale
9 geophysical electromagnetic measurements: *Inverse Problems*, **25**, 123012.
10
11

12 Adler, J., and O. Öktem, 2017. Solving ill-posed inverse problems using iterative deep neural
13 networks: *Inverse Problems*, **33**, v.1, 1-24.
14
15

16 Alpaydin, E., 2009, *Introduction to machine learning*: MIT Press.
17
18

19 Araya-Polo, M., J. Jennings, A. Adler, and T. Dahlke, 2018. Deep-learning tomography: The
20 Leading Edge, **37**, 58-66.
21
22

23 Archie, G. E., 1952. Classification of carbonate reservoir rocks and petrophysical considerations:
24 AAPG Bulletin, **36**, 218–298.
25
26

27 Bishop, C.M., 1995. Training with noise is equivalent to Tikhonov regularization: *Neural
28 Computation*, **7**, 108-116.
29
30

31 Colombo, D., G. McNeice, N. Cuevas, and M. Pezzoli, 2018. Surface to Borehole
32 Electromagnetics for 3D Waterflood Monitoring: Results from First Field Deployment: SPE
33 Annual Technical Conference and Exhibition, SPE-191544-MS.
34
35

1
2
3 Colombo, D., and G.W. McNeice, 2018. Surface to borehole CSEM for waterflood monitoring in
4 Saudi Arabia: Data analysis: SEG Technical Program, 868-872.
5
6

7
8
9 Colombo, D., and G. W. McNeice, 2017. Geophysical monitoring of waterflooding: methods and
10 perspectives, SEG Technical Program Expanded Abstracts, 1044-1048.
11
12

13
14
15 Colombo D., and G. W. McNeice, 2013. Quantifying surface-to-reservoir electromagnetics for
16 waterflood monitoring in a Saudi Arabian carbonate reservoir: *Geophysics*, **78**, E281–E297.
17
18

19
20
21 Colombo, D., V. Gitis, and R de Franco, 1997. Application of pattern recognition techniques to
22 long-term earthquake prediction in central Costa Rica: *Engineering Geology*, **48**, 7-18.
23
24

25
26
27 Commer, M., and G. A. Newman, 2008. New advances in three-dimensional controlled-source
28 electromagnetic inversion: *Geophysical Journal International*, **172**, 513-535.
29
30

31
32
33 Di, Haibin, M. Shafiq, and G. AlRegib, 2018. Multi-attribute k-means clustering for salt-boundary
34 delineation from three-dimensional seismic data: *Geophysical Journal International*, **215**, 1999-
35 2007.
36
37

38
39
40 Dogru, A. H., L. S. K. Fung, U. Middya, T. M. Al-Shaan, J. A. Pita, K. H. Kumar, H. J. Su, J.
41 C. T. Tan, H. Hoy, W. T. Dreiman, W. A. Hahn, R. Al-Harbi, A. Al-Youbi, N. M. Al-Zamel, M.
42 Mezghani, and T. Al-Mani, 2009, A next-generation parallel reservoir simulator for giant
43
44

1
2
3 reservoirs: SPE Journal Paper 119272 presented at the Reservoir Simulation Symposium in The
4
5 Woodlands, Texas.
6
7

8
9 Dosovitskiy, A., J.T. Springenberg, M. Riedmiller, and T. Brox, 2014. Discriminative
10
11 unsupervised feature learning with convolutional neural networks: NIPS, 766-774.
12
13
14

15
16 Goodfellow, I., Y. Bengio, and A. Courville, 2016. Deep learning, MIT Press.
17
18
19

20
21 Guillen, P., G. Larrazabal, G. Gonzales, D. Boumber, and R. Vilalta, 2015. Supervised learning to
22
23 detect salt body: SEG Technical Program, 1826-1829.
24
25

26
27
28 Guo, R., M. Li, F. Yang, and S. Xu, 2018. Application of supervised descent method for transient
29
30 EM data inversion: SEG Technical Program, 2126-2130.
31
32
33

34
35 He, Z., X. Liu, W. Qiu, and H. Zhou, 2004. Mapping reservoir boundary by using borehole-surface
36
37 TFEM technique: two case studies: EAGE Technical Program, P327.
38
39

40
41 Hornik, K., M. Stinchcombe, and H. White, 1989. Multilayer feedforward networks are universal
42
43 approximators: Neural Networks, **2**, 359-366.
44
45

46
47
48 Ji, S., W. Xu, M. Yang, and K. Yu, 2013. 3D Convolutional Neural Networks for Human Action
49
50 Recognition: IEEE Transactions on Pattern Analysis and Machine Intelligence, **35**, 221-231.
51
52

1
2
3 Kim, Y., and N. Nakata, 2018. Geophysical inversion versus machine learning in inverse
4 problems: The Leading Edge, **37**, 894-901.
5
6

7
8
9 Li, W., 2018. Classifying geological structure elements from seismic images using deep learning:
10 SEG Technical Program, 4643-4648.
11
12

13
14
15 Liang, L., A. Abubakar, and T. M. Habashy, 2016. Reservoir property mapping and monitoring
16 from joint inversion of time-lapse seismic, electromagnetic, and production data: Geophysics, **81**,
17 5, ID73-ID84.
18
19

20
21
22 Liu, G., F.A. Reda, K.J. Shih, TC. Wang, A. Tao, and B. Catanzaro, 2018. Image Impanting for
23 Irregular Holes Using Partial Convolutions: In: Ferrari V., Hebert M., Sminchisescu C., Weiss Y.
24 (eds.) Computer Vision – ECCV 2018. ECCV 2018. Lecture Notes in Computer Science, vol.
25 11215, 89-105. Springer.
26
27

28
29
30 Marsala, A., S. Ruwaili, S.M. Ma, Z. Ali, M. Buali, J.M. Donadille, S. Crary, and M. Wilt, 2008.
31 Crosswell Electromagnetic Tomography: from Resistivity Mapping to Interwell Fluid
32 Distribution: International Petroleum Technology Conference, IPTC 12229.
33
34

35
36
37 McNeice, G.W., and D. Colombo, 2018. 3D inversion of surface to borehole CSEM for waterflood
38 monitoring: SEG Technical Program, 878-882.
39
40

1
2
3 Oh, S., K. Noh, D. Yoon, S.J. Seol, and J. Byun, 2018. Salt Delineation from Electromagnetic
4 Data Using Convolutional Neural Networks: IEEE Geoscience and Remote Sensing Letters, **16**,
5 519-523.
6
7
8
9
10
11
12
13
14
15
16
17
18
19
20
21
22
23
24
25
26
27
28
29
30
31
32
33
34
35
36
37
38
39
40
41
42
43
44
45
46
47
48
49
50
51
52
53
54
55
56
57
58
59
60

Puzyrev, V., E. Vilamajó, P. Queralt, J. Ledo, and A. Marcuello, 2017. Three-dimensional modeling of the casing effect in onshore controlled-source electromagnetic surveys. *Surveys in Geophysics*, **38**, 527-545.

Ronneberger, O., P. Fischer, and T. Brox, 2015. U-net: Convolutional networks for biomedical image segmentation: International Conference on Medical image computing and computer-assisted intervention, 234-241, Springer, Cham.

Sietsma, J., and R.J.F. Dow, 1991. Creating artificial neural networks that generalize, *Neural Networks*, **4**, 67-79.

Streich, R., 2016. Controlled-Source Electromagnetic Approaches for Hydrocarbon Exploration and Monitoring on Land: *Surveys in Geophysics*, **37**, 47–80.

Tietze, K., O. Ritter, P. Veeken, 2015. Controlled-source electromagnetic monitoring of reservoir oil-saturation using a novel borehole-to-surface configuration: *Geophysical Prospecting*, **63**, 1468-1490.

Vilamajó, E., B. Rondeleux, P. Queralt, A. Marcuello, and J. Ledo, 2015, A land controlled-source electromagnetic experiment using a deep vertical electric dipole: experimental settings, processing, and first data interpretation: *Geophysical Prospecting*, **63**, 1527–1540.

Wang, W., F. Yang, and J. Ma, 2018. Velocity model building with a modified fully convolutional network: SEG Technical Program, 2086-2090.

Wilt, M. J., Alumbaugh, D. L., Morrison, H. E., Becker, A., Lee, Ki Ha, and Deszcz-Pan, M., 1995, Crosswell electromagnetic tomography: System design considerations and field results: *Geophysics*, **60**, 871- 885.

Xiong, X., and F. De la Torre, 2013. Supervised descent method and its application to face alignment. *Proceedings of the IEEE conference on computer vision and pattern recognition*, 532-539.

FIGURE CAPTIONS

Figure 1. Horizontal cross section through the reservoir representing the WAG process: a) baseline with only waterflooding active; b) 3-year time snapshot during WAG (water injection case and background waterflooding); c) 6-year time snapshot during WAG (gas injection case and background waterflooding). The two wells represent the simulated cross-well EM experiment with the well on the left being the injector and the J_z source, and the well on the right containing the multicomponent (E_z - H_{xyz}) receiver array.

Figure 2. Simulated cross-well experiment of WAG/EOR: (a, b, c) reservoir resistivity snapshots taken at three years interval with the first distribution representing the baseline waterflooding and the other two a case of water and gas injection during the WAG; (d, e) difference of resistivity relative to the baseline; (f, g) difference of E_z amplitudes relative to the baseline response.

Figure 3. Magnetic field components differences from baseline response: (a, b, c) distribution of Figure 2d, (d, e, f) distribution of Figure 2e.

Figure 4. 2D modified U-Net network model where the modification consists of removing the “copy and concatenate” operations of lower-level features.

Figure 5. Summary of the results: comparison of true and predicted models of the 20 samples left over for testing. E_z component only used for the training, validation and testing: 2 channel input

1
2
3 consisting of amplitude and phase of differential Ez (96x96x2) with one single channel in output
4
5 (192x192x1).
6
7
8
9
10
11
12
13
14
15
16
17
18
19
20
21
22
23
24
25
26
27
28
29
30
31
32
33
34
35
36
37
38
39
40
41
42
43
44
45
46
47
48
49
50
51
52
53
54
55
56
57
58
59
60

Figure 6. Comparison of inversion results for the same well couple with similar acquisition geometry and Jz-Ez components: (a, b) CO2 injection only and recovered model from L2 standard inversion; (c, d) WAG reservoir modeling and recovered model by ML-inversion using only the Ez component.

Figure 7. Model losses comparison for the case of training and validation with Ez only with the combination of Ez and Hx, Hy, Hz.

Figure 8. Prediction performance by using multiple EM components: a) true model, b) prediction with Ez component only, c) combination of Ez and Hx, Hy, Hz. The prediction using the full EM field is higher resolution and more accurate than the Ez component only.

Figure 9. Gaussian noise levels applied to the data and corresponding deep learning prediction. From top to bottom: first row is the no noise case, second row noise standard deviation is $10^{-9} \frac{V}{\sqrt{Hz}}$ (or $\frac{nT}{\sqrt{Hz}}$), third row $5 \cdot 10^{-9} \frac{V}{\sqrt{Hz}}$ (or $\frac{nT}{\sqrt{Hz}}$), fourth row $10^{-8} \frac{V}{\sqrt{Hz}}$ (or $\frac{nT}{\sqrt{Hz}}$). Prediction results on testing samples show good stability with increasing levels of noise showing only minor inaccuracies and distortions in the reconstruction.

Figure 10. Random partition dataset: training and validation losses at different noise levels.

1
2
3 Figure 11. Prediction performance with increasing levels of noise for the forward time
4 extrapolation example: true model vs predicted resistivity models.
5
6

7
8
9 Figure 12. Forward time extrapolation dataset: training and validation losses at different noise
10 levels.
11
12

13
14
15 Figure 13. Training and validation losses for mapping 3D resistivity models from 2D
16 electromagnetic field data.
17
18

19
20
21 Figure 14. Performance of 3D deep learning inversion of resistivity models: depth slices of true
22 and predicted models for WAG injection (left); 3D views of a portion of the true and predicted
23 models (right).
24
25

31 TABLE CAPTIONS 32 33

34
35
36 Table 1. Model prediction errors for different tests performed (only tests using all the EM
37 components are shown).
38
39
40

Model dimension	Noise level	Testing RMSm (Ohm·m)	
		Random partition	Forward extrapolation
2D	-	0.2751	0.3243
	$10^{-9} V/\sqrt{Hz}$	0.3369	0.3504
	$5 \cdot 10^{-9} V/\sqrt{Hz}$	0.3630	0.3861
	$10^{-8} V/\sqrt{Hz}$	0.3835	0.4870
3D	-	0.4205	-

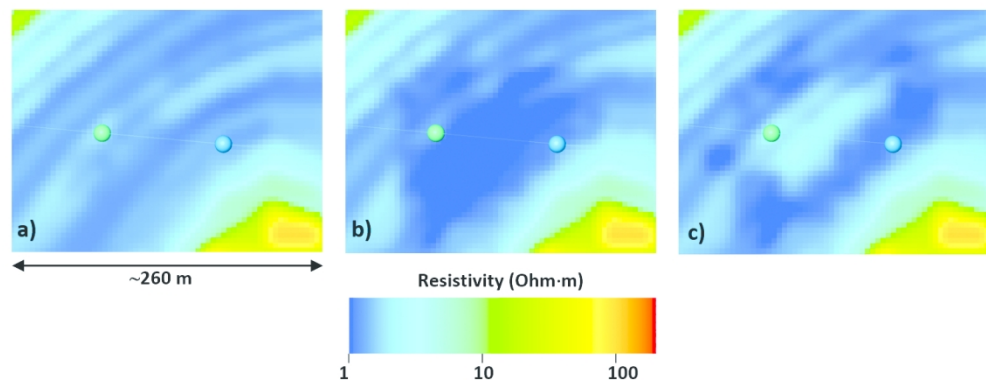


Figure 1. Horizontal cross section through the reservoir representing the WAG process: a) baseline with only waterflooding active; b) 3-year time snapshot during WAG (water injection case and background waterflooding); c) 6-year time snapshot during WAG (gas injection case and background waterflooding). The two wells represent the simulated cross-well EM experiment with the well on the left being the injector and the J_z source, and the well on the right containing the multicomponent (E_z - H_{xyz}) receiver array.

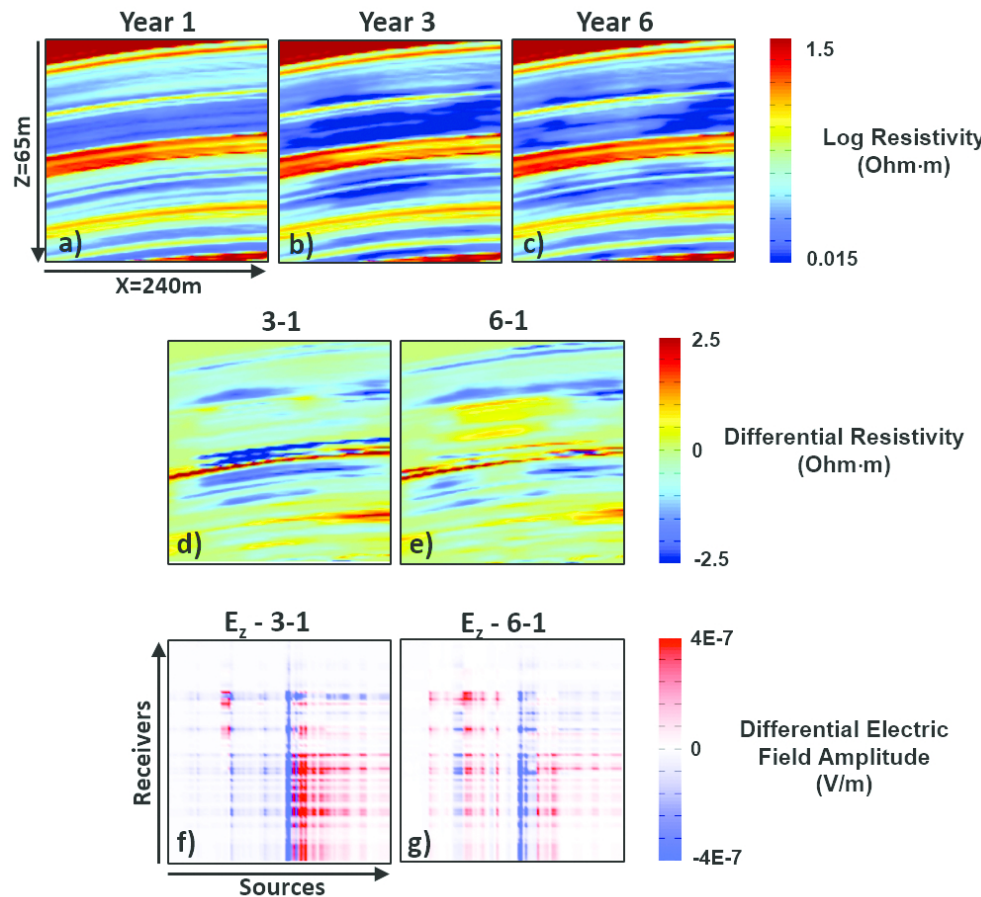


Figure 2. Simulated cross-well experiment of WAG/EOR: (a, b, c) reservoir resistivity snapshots taken at three years interval with the first distribution representing the baseline waterflooding and the other two a case of water and gas injection during the WAG; (d, e) difference of resistivity relative to the baseline; (f, g) difference of E_z amplitudes relative to the baseline response.

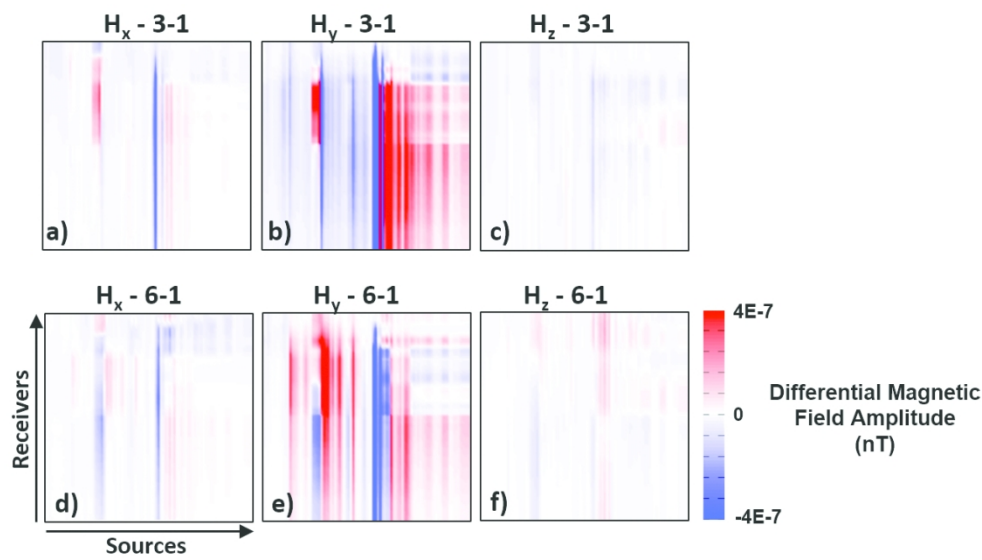


Figure 3. Magnetic field components differences from baseline response: (a, b, c) distribution of Figure 2d, (d, e, f) distribution of Figure 2e.

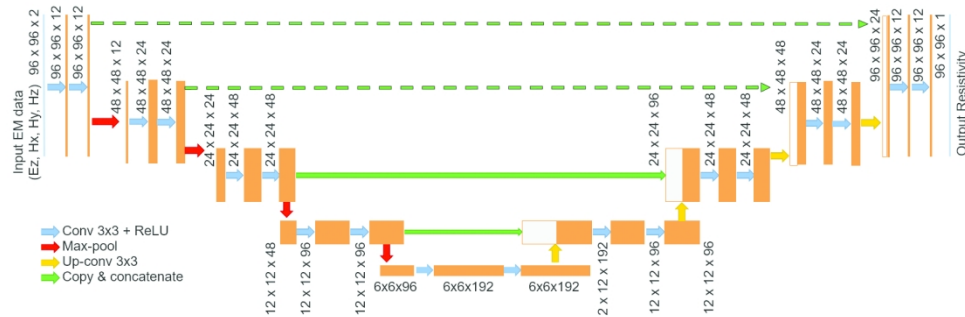


Figure 4. 2D modified U-Net network model where the modification consists of removing the “copy and concatenate” operations of lower-level features.

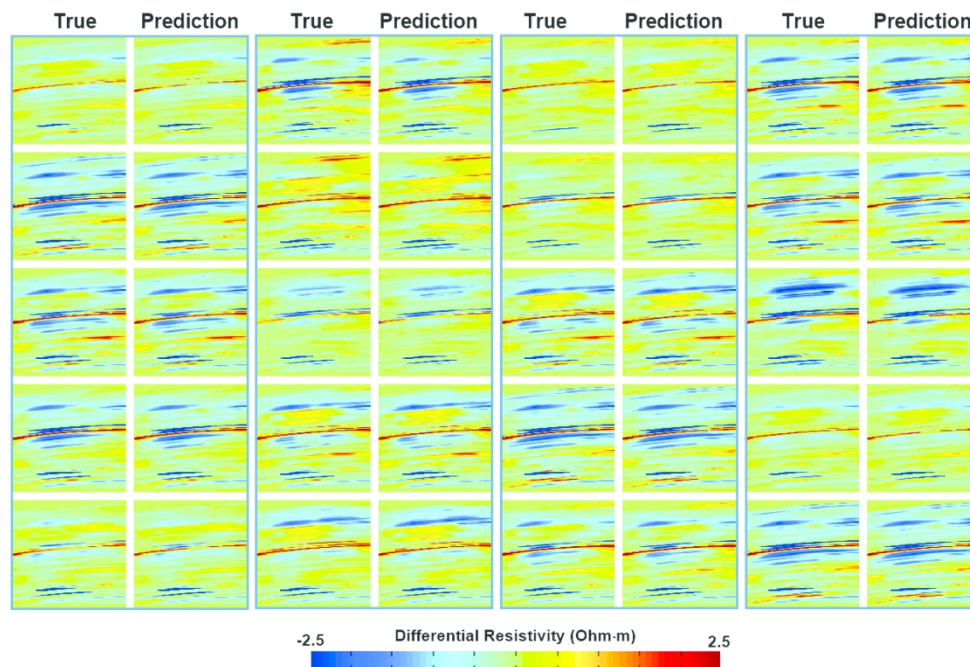


Figure 5. Summary of the results: comparison of true and predicted models of the 20 samples left over for testing. Ez component only used for the training, validation and testing: 2 channel input consisting of amplitude and phase of differential Ez ($96 \times 96 \times 2$) with one single channel in output ($192 \times 192 \times 1$).

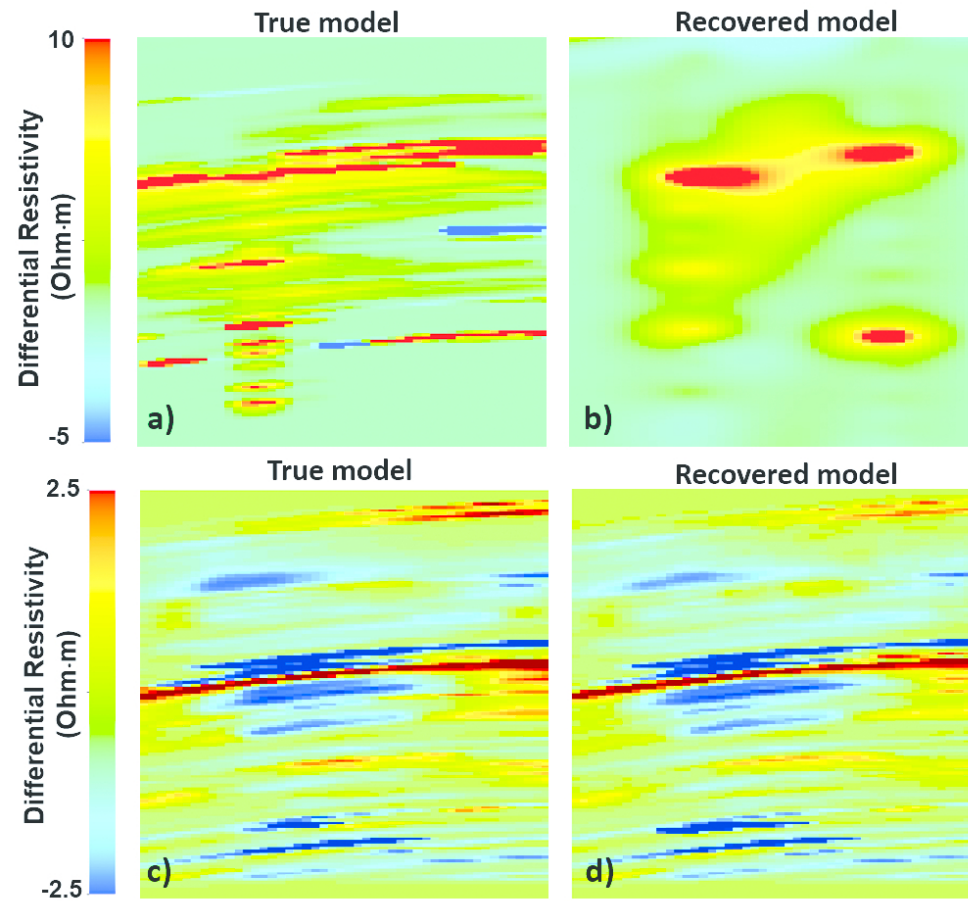


Figure 6. Comparison of inversion results for the same well couple with similar acquisition geometry and J_z - E_z components: (a, b) CO₂ injection only and recovered model from L2 standard inversion; (c, d) WAG reservoir modeling and recovered model by ML-inversion using only the E_z component.

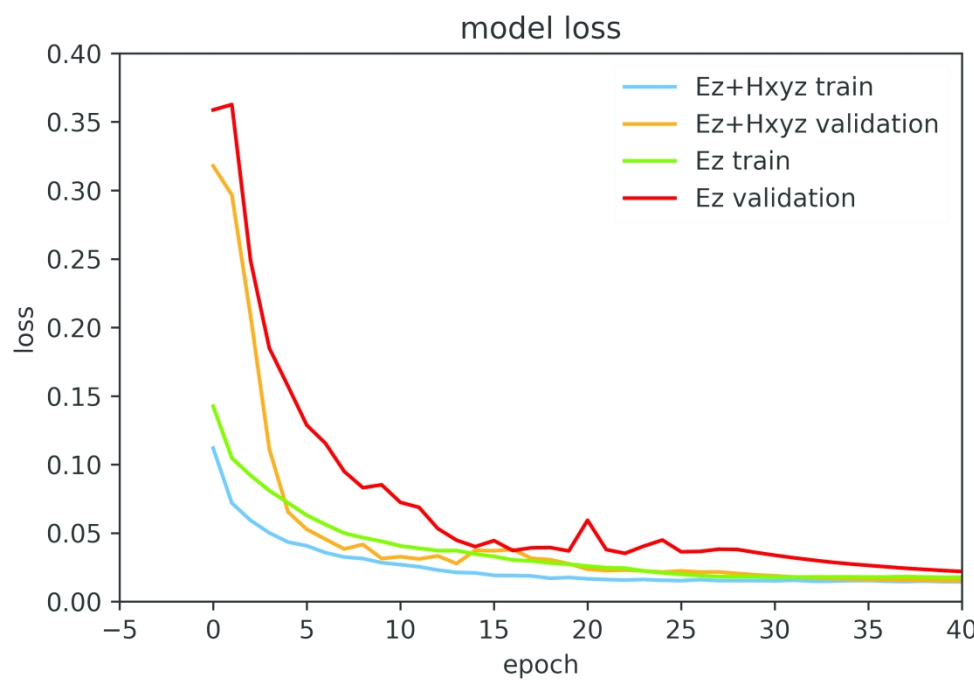


Figure 7. Model losses comparison for the case of training and validation with Ez only with the combination of Ez and Hx, Hy, Hz.

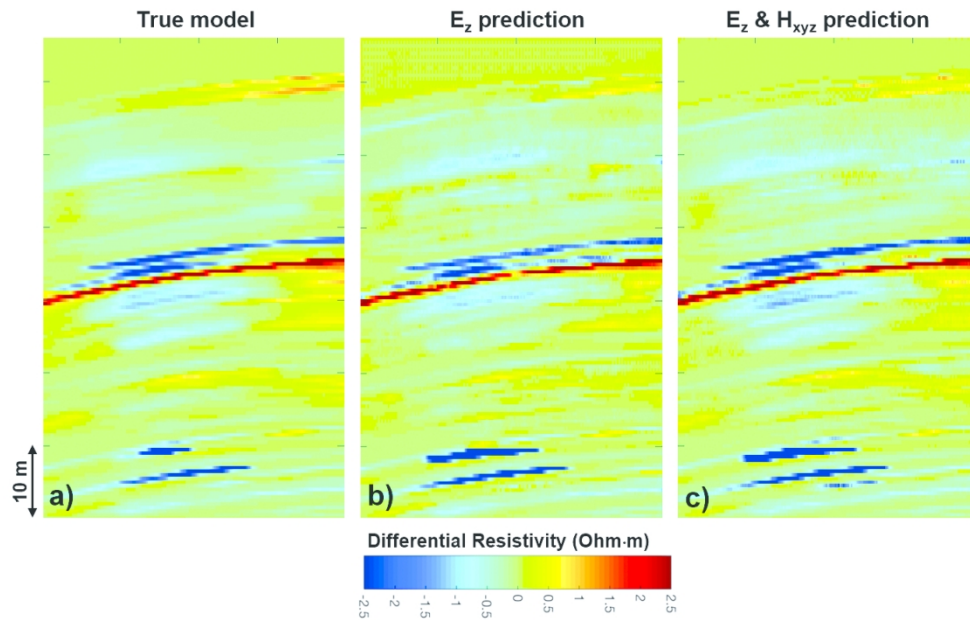


Figure 8. Prediction performance by using multiple EM components: a) true model, b) prediction with E_z component only, c) combination of E_z and H_x, H_y, H_z. The prediction using the full EM field is higher resolution and more accurate than the E_z component only.

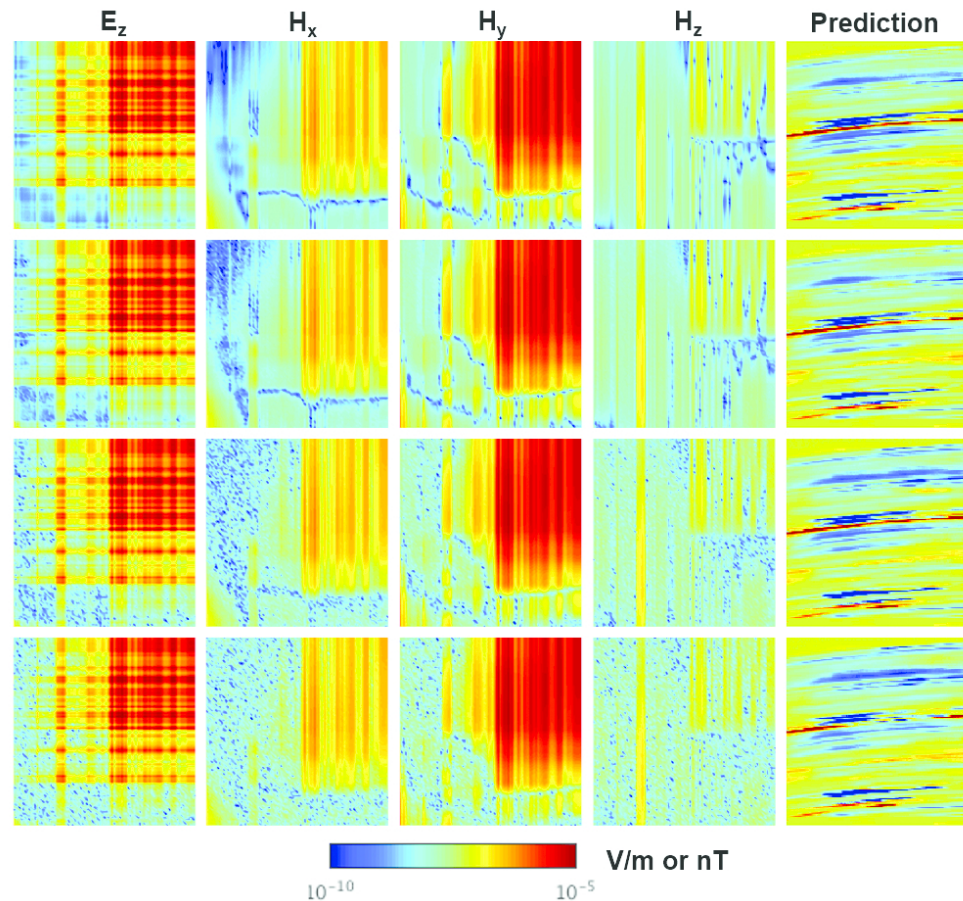


Figure 9. Gaussian noise levels applied to the data and corresponding deep learning prediction. From top to bottom: first row is the no noise case, second row noise standard deviation is $10^{-9} \text{ V}/\sqrt{\text{Hz}}$ (or $\text{nT}/\sqrt{\text{Hz}}$), third row $[5\text{--}10]^{-9} \text{ V}/\sqrt{\text{Hz}}$ (or $\text{nT}/\sqrt{\text{Hz}}$), fourth row $10^{-8} \text{ V}/\sqrt{\text{Hz}}$ (or $\text{nT}/\sqrt{\text{Hz}}$). Prediction results on testing samples show good stability with increasing levels of noise showing only minor inaccuracies and distortions in the reconstruction.

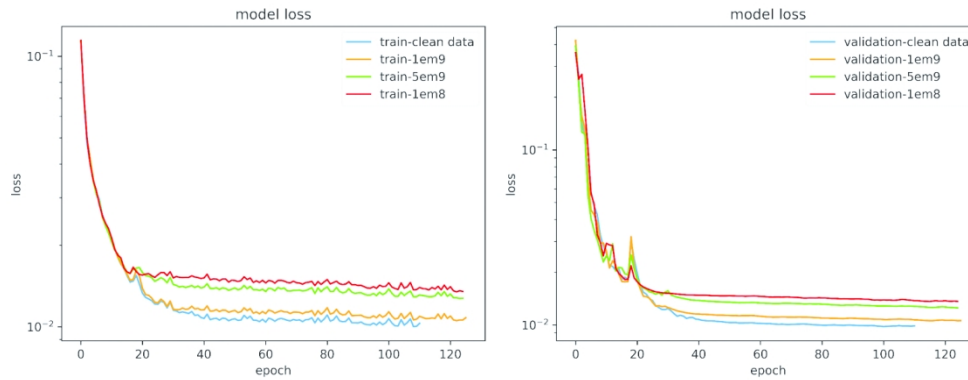


Figure 10. Random partition dataset: training and validation losses at different noise levels.

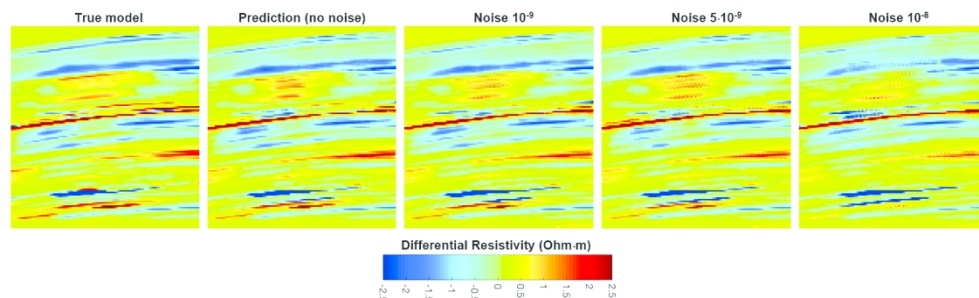


Figure 11. Prediction performance with increasing levels of noise for the forward time extrapolation example: true model vs predicted resistivity models.

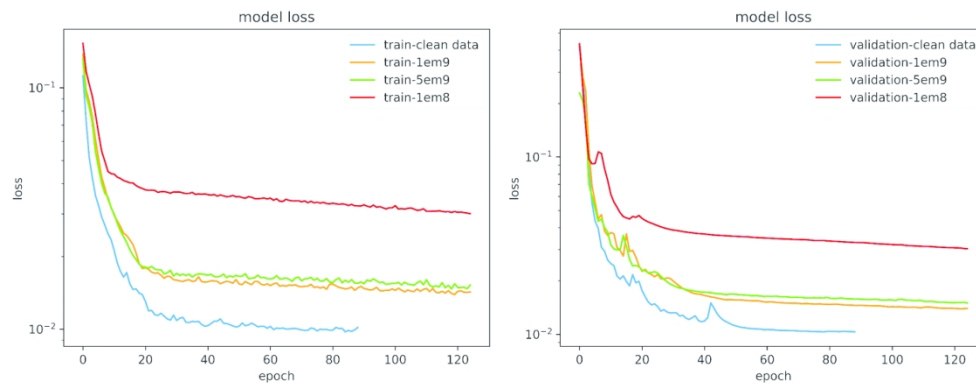


Figure 12. Forward time extrapolation dataset: training and validation losses at different noise levels.

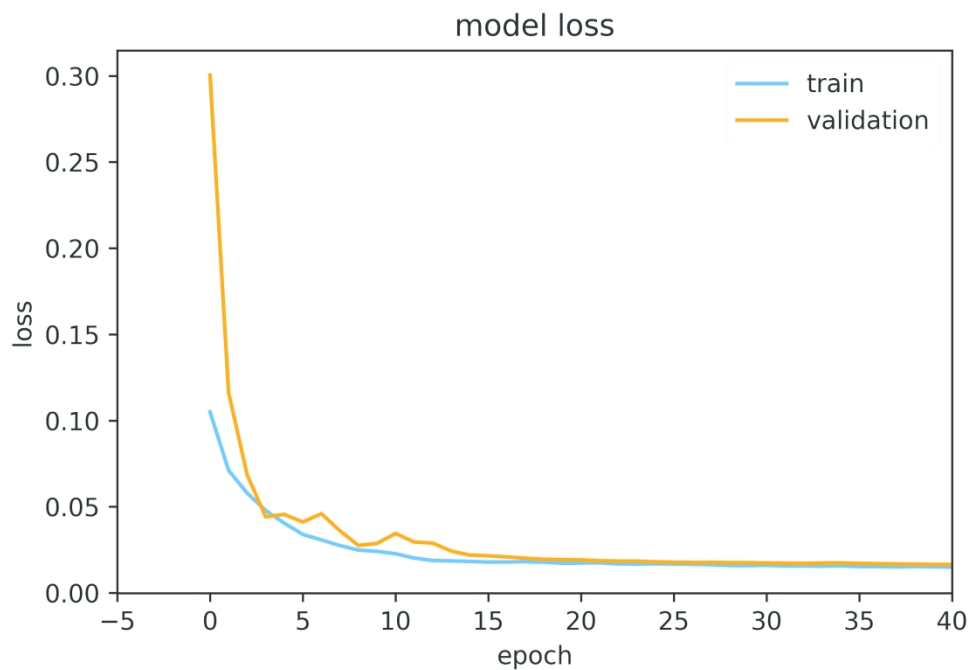


Figure 13. Training and validation losses for mapping 3D resistivity models from 2D electromagnetic field data.

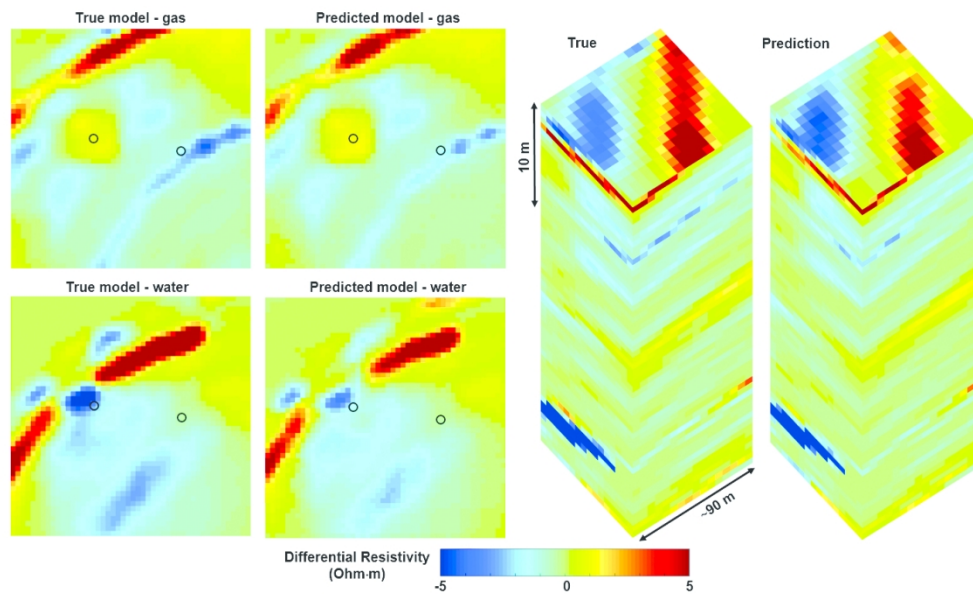


Figure 14. Performance of 3D deep learning inversion of resistivity models: depth slices of true and predicted models for WAG injection (left); 3D views of a portion of the true and predicted models (right).

DATA AND MATERIALS AVAILABILITY

Data associated with this research are confidential and cannot be released.